SiO_x-Rich Electrode Directly Optimized Using Key Formulation Parameters

Clément Meyssonnier, Cassandre Chalard, Amina Merabet, Nicolas Goubard-Bretesché, Nicolas Dupré, Cyril Paireau, Bernard Lestriez

SiO_x-rich electrode directly optimized using key formulation parameters

Clément Meyssonnier[1,2], Cassandre Chalard[1,2], Amina Merabet[1], Nicolas Goubard-Bretesché[1], Nicolas Dupré[1], Cyril Paireau[2], Bernard Lestriez[1]

[1] Nantes Université, CNRS, Institut des Matériaux de Nantes Jean Rouxel, IMN, Nantes F-44000, France
[2] Armor Battery Films, 7 Rue de la Pelissière - 44118 La Chevrolière
bernard.lestriez@cnrs-imn.fr

Abstract Text

The use of key parameters of the SiO_x/graphite electrode formulation, and their critical values, makes it possible, without any trial-and-error type experimentation, to identify optimal electrode formulations for different SiO_x/graphite mass ratios ranging up to 40:60. From the first attempt, electrodes presenting good cyclability at high surface capacity of 5.2 mA h cm^{-2} were formulated, reaching for example more than 93% capacity retention after 60 cycles in a full cell, with an electrolyte rich in FEC and EC-free, however with a prelithiation strategy. With a positive electrode based on NMC_{811}, the gains in volumetric energy and power density are + 18 and + 28% compared to graphite, considering only the electrode volumes. The principle of using the key electrode formulation parameters introduced here is expected to accelerate and facilitate the optimization of electrode formulations.

1. Introduction

Mixtures of graphite and silicon-based materials usable as a negative electrode are the subject of intense research and development with the aim of increasing the energy density of Li-ion batteries.[1] The specific capacity of such a mixture is determined by the graphite/silicon-based material ratio and by the nature of the latter. The silicon "component" can be in an oxidized form (SiO_x with x~1), in the form of an alloy with inactive elements (Si@M), and/or intimately associated with carbon or graphite in the form of composite material (Si@C or Si@G).[2] High specific capacity can improve volumetric energy density by reducing active material mass loading and thus electrode thickness for a comparable electrode density. However, due to the considerable volume changes associated with the alloying reaction of silicon with lithium, the increase in specific capacity poses a risk of

significant electrode swelling and instability during cycling.[3],[4],[5] It is then necessary to improve the resiliency of the electrode to silicon's volume variations by optimizing the formulation of the electrode, via the choice of the nature and quantity of the additives (polymer binder and electronic conductive agent),[6],[7],[8],[9],[10],[11] and by adapting the morphology of the graphite[12],[13],[14] Furthermore, due to the different (de)lithiation potentials of graphite and silicon, the operating voltage of a lithium-ion cell integrating this type of negative electrode varies with its specific capacity. High silicon content in the electrode decreases the operating voltage of the cell. Therefore, to achieve high volumetric energy density, it is then important to optimize the graphite/silicon material ratio in the negative electrode using this mixture. With this dual objective of optimizing and rationalizing the formulation of negative electrodes based on silicon and graphite, we recently proposed using two parameters fixing the proportions of the constituents of the electrode relative to each other.[15],[16]

The first parameter makes it possible to determine the quantity of binder relative to the quantity of the other powdery constituents, namely the active material(s) and the conductive additive(s). This parameter is given by the following equation,

$$\Gamma = \frac{binder\ mass\ (mg)}{powders\ surface\ area\ (m^2)} \quad (1)$$

where Γ (in mg m^{-2}) is the binder-to-powders coverage ratio. It is based on micromechanical models developed in the field of polymeric composite materials and on the fact that the cohesion of the electrodes is ensured by the formation of sticky bridges between the particles by the binder, which is distributed on the surface developed by these particles during the manufacture of electrodes. It is therefore expressed as the mass (or volume) of binder relative to the quantity of surface area offered by all the powders, calculated considering their weight fraction in the electrode and their specific surface area. The second parameter makes it possible to determine the quantity of graphite and conductive additive relative to the quantity of silicon, and is given by the following equation,

$$\Omega = \frac{powders\ surface\ area\ of\ graphite\ \&\ conductive\ carbon\ (m^2)}{powders\ surface\ area\ of\ SiO_x\ (m^2)} \quad (2)$$

where Ω is the carbons to silicon ratio. It is based on the obvious importance of contacts

between the different types of particles on maintaining electrical connectivity within the electrode which is undermined by variations in silicon volume. Statistically, a greater number of contacts or a larger contact area between the two phases should allow longer durability of the connectivity between the two phases during cycling. The amount of contact between the two phases depends both on the amount of surface area deployed by each phase, and on the porosity. As the role of porosity on the quantity of contact is not easily calculated, we worked with electrodes of similar porosity and typical of industrial application. Thus, the comparison between the quantity of contacts between the two phases between different electrodes can be made with the ratio of surfaces developed by each phase. The higher it is, the more contacts will be statistically numerous between the graphitic phase and the SiOx phase. Our recent work on SiO_x/graphite electrodes (weight balance 23:77) has shown that there are critical values of these two parameters to reach a good cyclability. There are even optimal values, 17 mg_{binder} $m^{-2}_{SiOx+Gr+C}$ and 20 m^2_{Gr+C} m^{-2}_{SiOx}, for electrodes with a porosity around 35%, to maximize both gravimetric and volumetric capacities, and behaviour at high current regime (power).[15],[16]

The objective of this new work was to study the predictive value of these parameters. Namely, is it possible, based on the optimal values of these parameters for a state-of-the-art electrode, to identify *a priori* the formulation of an electrode comprising a novel element? For example, a new electroactive material different in its morphological characteristics or its specific capacity, a new conductive additive, a new binder... The potential for extrapolation of these two parameters is evaluated here on SiO_x/graphite electrodes whose SiO_x content is increased (weight balance 30:70 and 40:60) compared to that (23:77) for which the two parameters were optimized. Remarkably, this approach makes it possible to prepare electrodes with equal cyclability, despite the increase in the SiO_x content, while the state of the art generally shows a deterioration in cyclability when an electrode is enriched in the silicon-based material.[17],[18],[19]

The paper is thus organized into three parts. First of all, we study the cyclability in half cells of SiO_x/graphite electrodes with variable SiO_x content and whose formulation is determined with the same optimized values of the two parameters Γ and Ω. Then, the power behaviour of

these electrodes is studied, the question being that if silicon-based materials can increase the gravimetric, volumetric capacities and energy density of Li-ion batteries, how do they affect the charge/discharge rates and power density? Finally the cyclability of the SiO_x/graphite electrodes is compared to that of state-of-the-art graphite in full cells.

2. Experimental

2.1 Materials

All electrode components are industrial grades. The silicon-based material is a silicon oxide covered by graphene sheets (SiO_x) from a graphene supplier (D50 ≈ 10 µm, specific surface area ≈ 1.4 $m^2 g^{-1}$, specific capacity ≈ 1400 mA h g^{-1}). Graphite active materials used are spherical graphite GHDR 15-4 (D50 = 17 µm, specific surface area ≈ 4 $m^2 g^{-1}$ – Imerys) and flake graphite SFG6L (D90 = 5.3 - 7.3 µm, specific surface area ≈ 17 $m^2 g^{-1}$ – Imerys) with a theoretical capacity of 372 mA h g^{-1}. C-NERGY™ SUPER C45 was used as conductive carbon additive (grit 20 µm = 12 ppm, specific surface area ≈ 45 $m^2 g^{-1}$ – Imerys). A commercial solution containing carbon nanotubes (CNT) dispersed in water and carboxymethylcellulose (CMC) was used. CNT are Graphistrength® C W2-L C from Arkema (specific surface area ≈ 220 $m^2 g^{-1}$). CMC is considered as a binder. PolyAcrylic acid (PAA, Mw = 450 000 g mol^{-1} - Sigma-Aldrich) lightly neutralized with a $LiOH.H_2O$ salt (Sigma-Aldrich, white crystal) was used as binder. In addition, the Styrene-Butadiene Rubber (SBR – BM-451B) from Zeon Corporation was used to complete PAA. Electrode graphite reference are composed of graphite GHDR 10-4 (D50 = 12 µm, specific surface area ≈ 4.7 $m^2 g^{-1}$ – Imerys), WALOCEL™ CRT 2000 PA Sodium Carboxymethylcellulose (CMC) from Dow®, same SBR and C45 than SiO_x-based electrodes.

2.2 Electrodes preparation

Details of anodes composition are gathered in Table 1. Binder solutions for SiO_x/Graphite anode were prepared by mixing PAA and water with a magnetic stirrer. As shown in Table 1, the binder amount has been varied from a slurry to another. We adapted the binder concentration between 5-7 wt% of this solution to work at quite similar viscosity. The pH of PAA solutions was adjusted at 4.0 ± 0.1 with the $LiOH.H_2O$ salt. However, it is likely

that the neutralization of –COOH moieties of PAA by LiOH is a slow process and that the actual pH after mixing the electrode slurry is lower than that. The PAA dissociation level is low, about 5%. CNT solution was added to the binder solution if appropriate. pH of water/CMC solution was not adjusted.

Electrode slurries were prepared by mixing the binder solution with other electrode components thanks to a planetary blender (Thinky mixer ARE 250). Pure graphite electrode slurries were prepared by mixing CMC binder solution, GHDR 10-4, C45 and SBR in commercial proportion as anode reference. Three different SiO_x/Graphite balance were tested 23:77, 30:70 and 40:60. The powder of each electrode component was incorporated successively, and binder solution was then progressively added to form the electrode slurry. An example of such process is given in Table S1. The slurry was coated onto an 8 µm copper foil and dried according to the following stages: 10 min. at 30°C, a subsequent temperature ramp to reach 110°C in ≈ 35 min. and finally 30 min. at 110°C. The wet thickness was adapted for each slurry to obtain a theoretical surface capacity of 5.2 ± 0.1 mA h cm^{-2}. After the drying step, electrodes were then calendered at 1.5 t cm^{-2} with a rolling press (Medlab P – Ingecal) at 50°C to reach a porosity between 30 and 40%. Porosity was calculated from the components mass fractions and densities thanks to three thickness measurements of each electrode by a micrometer (Mitutoyo).

NMC cathode slurries were prepared by mixing PVdF binder solution, carbon black and NMC active material during 90 min. in a stirring machine (ultra turrax® - IKA) following steps detailed in Table S2. Electrodes were coated onto a 15 µm aluminium foil and dried from 65°C to 130°C during 75 min. and then 60 min. at 130°C under vacuum. Electrodes were then calendered at 0.5 t cm^{-2} to reach a porosity between 30 and 40%.

Finally, 15 mm diameter circular (negative and positive) electrodes were punched out and dried 3-4 hours at 100°C under vacuum in a Büchi before entering the glove box and coin cell assembling.

2.3. Electrochemical measurements

Half-Cell Li || SiO_x/Gr. Electrodes were tested in coin cell versus metallic lithium.

They were assembled in glove box under argon atmosphere. A glass-fibre Whatman GF/D and a trilayer microporous membrane (PP/PE/PP) Celgard H2010 were used as separators. They were soaked with 200 µL electrolytic solution of 1 M $LiPF_6$ in ethylene carbonate (EC) and dimethyl carbonate (DMC) 1:1 + 10 wt% fluoroethylene carbonate (FEC). SiO_x/Graphite electrodes were employed as the working electrodes with lithium foil as both counter and reference electrodes. The cycling tests were performed in galvanostatic mode at 23°C within the potential window of 1 – 0.01 V versus Li^+/Li. The theoretical rate based on the nominal capacities of SiO_x and graphite (1400 and 360 mA h g^{-1} respectively) was fixed at C/20 for the first three cycles (full capacity in 20h). The third cycle was then used to define the experimental capacity of the SiO_x/Graphite electrode in order to apply a real C-rate for next cycles.

Cyclability. A first series of cells was tested to evaluate the cyclability at a rate of C/5 (for both charge and discharge) for the next 57 cycles after the three cycles of formation. For all cycles, a constant current (CC) followed by a constant voltage (CV) step at the end of the SiO_x/Graphite electrode lithiation are applied. This floating step at 10 mV was maintained until the measured current reached an equivalent of a C/50 value or for a maximum duration of two hours. For the sake of reproducibility, at least two cells were tested for each SiO_x/Graphite electrode formulation, and the results were averaged and standard deviation shown.

Effect of the Discharge/Charge rate (D/C-rate). A second series of cells was tested to evaluate D/C-rate effect. The three cycles of formation were applied and then from cycle 4 to 34, we evaluated the effect of the rate during delithiation noted D-rate. Lithiation, noted C-rate, remained at C/5 with a CV period to be limited only by the effect of delithiation. Blocks of fives cycles at D/5, D/2, 1D, 2D and 3D were carried out with a final block of three cycles at D/5 with CV. A complete cycle at D/5-C/5 was carried out between each block to check that the D-rate increase did not degrade the electrode. Finally, the last delithiation of each block was completed by a delithiation at D/5 in order to apply a treatment on the incremental capacities data (dQ/dV) as explained in the corresponding section. From cycle 35 to 67, we did the same process but on the lithiation with constant D/5 delithiation. In order to

properly evaluate the effect of the C-rate in lithiation, the CV step was suppressed at the cut-off potential of 10 mV. An initial block of 3 cycles at C/5 was carried out, followed by blocks of five cycles at C/2, 1C, 2C and 3C, separated by a complete cycle at D/5-C/5 with CV to check the integrity of the electrode. Finally, six cycles at D/5-C/5 were performed at the end. Three without CV period and three with.

Analysis of incremental capacity curves. Derivative of the capacity with respect to the voltage data were calculated using the EC-Lab® software (BioLogic). A post-processing of these data was done with a home-made routine written using Python™. The aim of the routine was to treat automatically a significant amount of data to discriminate the capacity contributions of each active material. More details are given in Supporting Information.

Full cells SiO_x/Gr || NMC_{811}. SiO_x/Graphite electrodes were tested in coin cell versus NMC_{811} cathode. The electrolytic solution was 1 M $LiPF_6$ in FEC:DMC 3:7, separator Whatman GF/A soaked with 95 µL. The same cycling sequence was used with respect to half-cell tests, within a 2.5 - 4.2 V potential window. A CV step at 4.2 V was also used to reach complete lithiation of the SiO_x/Graphite anode until the measured current reached an equivalent of a C/20 value or a duration of more than two hours. All SiO_x-based anodes were previously pre-lithiated versus metallic lithium with the same electrolyte to achieve a relevant comparison with recent industrial approaches.[20] Practically, they were first assembled in a half-cell configuration to carry out an initial cycle of formation at D/20-C/20 as described above. This methodology allows eliminating the significant initial irreversible capacity typically observed for Si/Gr anodes[15] caused by the low initial coulombic efficiency of ≈ 50-70% of SiO_x material.[21] Half-cells were then opened to collect the pre-lithiated SiO_x/Gr anodes in their delithiated state. They were then washed with DMC and dried one day in glove box. They were reassembled in coin cells versus NMC cathodes. The theoretical capacities ratio between the negative and positive electrode (N/P) is equal to 1.15 ± 0.01 by using 360 mA h g^{-1}_{Gr} for graphite material, 1400 mA h g^{-1}_{SiOx} for SiO_x and 204 mA h g^{-1}_{NMC} for NMC_{811}. A ratio specifically higher than 1 was chosen to prevent lithium plating deposition on the negative electrode, especially during the first delithiation of the NMC.

Direct Current Internal Resistance (DCIR). This electrochemical method allows an

easy and direct access to the internal resistance of the cell during cycling. Measurements were performed at D/5-C/5 rate and during SiO_x/Gr delithiation step to prevent lithium plating. A current pulse was applied at a potential of 210 mV and 3.6 V, in half-cell and in full-cell configuration, respectively. The current is then increased from D/5 to 1D rate for one second to measure only electronic resistance (restricted to phenomena with kinetics up to 1 Hz). The internal resistance is deduced from the ratio between de voltage drop (ΔV) and the current drop (ΔI).

2.4 Electrical measurements

1.5 diameter electrodes were cropped and calandered with a press to reach four different porosities between 10 and 50% per composition. Three measurements of resistivity were done per samples with the electrode resistance measurement system HIOKI – RM2610. This device uses the 4-point probe method and employs numerical analysis using the finite volume method to calculate electrode sheets' composite layer volume resistivity (Ω cm) and the interface (contact) resistance (Ω cm²) between the composite layer and the collector. More information can be found in the SI.

2.5 Scanning electron microscopy (SEM) & Cross section preparations

To observe the morphology of the electrodes before cycling, cuts were made using a cross section polisher (JEOL SM-09010). Then a scanning electron microscope (SEM – JEOL JSM 7600F) was used to visualize the electrode morphology along the electrode depth. Cycled electrodes were rinsed by immersion in DMC under argon atmosphere prior to observation and directly transported in the scanning electron microscope without air exposure. Cuts were made using FIB/SEM ZEISS Cross Beam 550 FIB.

Table 1: Weight percentage composition of the electrodes and their contact and coverage ratio.

Name	Γ[a]	Ω[b]	δ[c]	SiO_x/Gr	SFG6L/GHD	Binder [wt%]			Active materials [wt%]			C45[c]	CNT
y-SiO_x series	[mg m^{-2}]	[m² m^{-2}]	[m² m^{-2}]	balance	R balance	PAA+CMC[d]	SBR	LiOH	SiO_x	SFG6L	GHDR	[wt%]	[wt%]
Graphite	07.0	/	0.10	000:100	000:100	00.0 +1.0	2.5	/	/	/	95.5	1.0	/
23-SiO_x	14.5	21.8	0.65	23:77	10:90	06.3 +0.6	2.5	0.08	19.9	06.7	60.3	3.1	0.5
30-SiO_x	14.7	21.8	0.65	30:70	28:72	08.5 +0.7	2.5	0.10	25.1	16.4	42.1	3.9	0.6
40-SiO_x	14.5	21.8	0.66	40:60	60:40	11.3 +1.0	2.5	0.14	31.7	28.6	19.0	4.9	0.8

[a] Coverage ratio, equation (1).

[b] Carbons to silicon ratio, equation (2).

[c] Percolation ratio, equation (3).

[a, b, c] Powders surface area were estimated from their BET surface area and their respective mass in the electrode.
[d] PAA %wt +CMC %wt. CNT are dispersed in commercial solution containing CMC.

3. Results and discussion

3.1 Physical properties

Table 1 gives the electrodes compositions. Four different formulations are compared. A graphite electrode (reference), whose formulation is typical of the state of the art and SiO_x/graphite electrodes with varying ratios (weight balance 23:77, 30:70, and 40:60). The quantity of binder (PAA, CMC and SBR) is adjusted so that the coverage ratio value is equal to 14.5-14.7 $mg_{binder}\ m^{-2}_{SiOx+Gr+C}$ in these last three electrodes. The quantity of SBR is limited to 2.5 wt%, because beyond that the electrodes show kinetic limitations.[15] The CMC is provided by the CNT suspension used as a conductive additive. The mixture of graphites (GHDR 15-4 and SFG6L) and conductive carbons (C45 and CNT) is also in variable proportion but adjusted so that the carbons to SiO_x ratio value is equal to 21.8 $m^2_{Gr+C}\ m^{-2}_{SiOx}$. As there are several ways to set the value of the carbons to silicon ratio Ω, by playing both on the proportion of the two graphites, and of the conductive additives, we have introduced a third arbitrary formulation parameter, which sets the quantity of conductive additive in proportion to that of the electroactive materials, considering for this their respective developed surfaces, according to equation 3

$$\delta = \frac{powders\ surface\ area\ of\ conductive\ carbon\ (m^2)}{powders\ surface\ area\ of\ active\ materials\ (m^2)} \quad (3)$$

When the quantity of SiO_x is increased, to keep the carbons to silicon ratio constant it is necessary to increase the proportion of SFG6L relative to that of GHDR15-4. As a result, the total surface area developed by these 3 powders increases, which as a consequence of equation 3, leads to an increase in the proportion of conductive additive. In summary, the 23-SiO_x formulation was optimized in our previous work, while the ones of 30- and 40-SiO_x were calculated by setting the different ratios, Γ, Ω, and δ to their respective values (which are given in Table 1). A simple iteration process allows to converge towards a solution giving an electrode formulation such that the compositions of the different constituents satisfy the

above conditions.

SEM observations make it possible to assess the morphology of the electrodes (Figure 1 a-b). On the images in backscattered electron mode, the copper current collector and the SiO_x particles appear in light grey. GHDR 15-4 graphite particles are distinguished by their large spherical shape (average diameter 17 µm) and SFG6L graphite particles by their platelet shape. The principle of formulation of these electrodes is partly illustrated in these images where we can see that the SFG6L content is higher in the 40-SiO_x electrode than in 23-SiO_x in order to keep the carbons to silicon ratio Ω constant.

We can also see, on the images in secondary electron mode, the higher content of conductive additive in the 40-SiO_x electrode. PAA, CMC and SBR binders are however impossible to distinguish. We also observe that the nature of the porosity is different, with larger pores in 23-SiO_x, due to the greater content of large GHDR 15-4 particles.

Table 2 lists the different parameters of *y-SiO_x* electrodes. As we have decided to work with a constant areal capacity of ≈ 5.2 mA h cm^{-2}, the mass loading of active material naturally decreases as the SiO_x content increases in the electrode. Electrode thickness is decreasing too because of the quite similar values of porosity of all electrodes, ≈36%, even though size of pores and shapes are different between these electrodes. Such a decrease in thickness would clearly be an advantage for SiO_x-based electrode, allowing *a priori* for easier electrolyte impregnation, faster ionic diffusion throughout the thickness of the electrode, as well as higher gravimetric and volumetric capacities, which will be assessed later.

Table 2: Typical characteristics of y SiOx electrodes series: areal capacity, mass loading, electrode thickness and calculated porosity at pristine state.

Name	Initial areal capacity [mA h cm^{-2}]	Mass loading of Active Mat. [mg_{AM} cm^{-2}]	Electrode thickness [µm]	Initial porosity [%]
Graphite	5.00 ± 0.00	13.8 ± 0.2	105 ± 4	36 ± 4
23-SiO_x	5.19 ± 0.04	08.3 ± 0.1	071 ± 3	36 ± 3
30-SiO_x	5.36 ± 0.05	07.6 ± 0.1	069 ± 5	37 ± 5
40-SiO_x	5.29 ± 0.01	06.5 ± 0.0	060 ± 2	34 ± 2

Electrical resistivity of the composite electrodes and their contact resistance at the interface with the current collector are displayed in Figure 2 a and b, as a function of the porosity. The

latter was varied on purpose to better see trends. For all compositions, the electrical resistivity tends to decrease with the porosity reduction, as the more the particles are tightly packed, the more the number of contacts between particles increase, thus favouring electrons transfer.[22],[23] In the case of the graphite reference, this impact is obviously stronger, with an electrode resistivity dropping from $1.30\times10^{-1} \pm 0.15\times10^{-1}$ Ohm cm at 38% of porosity to $0.26\times10^{-1} \pm 0.03\times10^{-1}$ Ohm cm at 21% of porosity. This is likely congruent with the low number of contact points between graphite particles due to their large sizes and the low content of C45 carbon black. However, the resistivity of this electrode is lower than SiO_x-based one's, likely due to the larger amount of insulating SiO_x amount in the latter ones. Resistivity values are quite similar for 23-, 30- and 40-SiO_x, which can be attributed to their similar percolation ratio δ ($= 0.65\ m^2_{C+CNT}\ m^{-2}_{SiOx+Gr}$). The larger amount of conductive additives compensates for the larger amount of SiO_x. Resistivity ranges from $0.65\times10^{-1} \pm 0.07\times10^{-1}$ Ohm cm at ≈ 14% porosity to $1.5\times10^{-1} \pm 0.60\times10^{-1}$ Ohm cm at ≈ 31%. However, at higher porosity, resistivity values diverge and increase with the content of SiO_x material. Such a change in behaviour is attributable both to the increase in the number of particles||binder||particle interfaces caused by SFG6L and C45 increase (SFG6L, C45 and binder contents increase concomitantly as shown in Table 1) and the more porous structure. Finally, in the porosity window of electrodes tested in batteries (32%-40%), we observe a small increase in the resistivity with increasing SiO_x content (from 0 to 40 wt%). This one remains low as the values vary between 0.1 and 0.2 Ohm cm.

Figure 2b shows the contact resistivity between the composite electrodes and the copper current collector. Values are mostly independent from the porosity for 23-, 30- and 40-SiO_x electrode (≈ 1.1×10^{-3} Ohm cm² at ≈ 14% of porosity and ≈ 1.3×10^{-3} Ohm cm² at ≈ 50%). On the opposite, the graphite electrode is very sensitive to the porosity, as shown by the increase from ≈ 4.3×10^{-3} Ohm cm² to ≈ 13×10^{-3} Ohm cm² between 21% and 38% porosity. The contact resistivity for graphite electrode is also clearly higher than those measured for the other *y-SiO$_x$* electrodes, which is likely due to their composition with only large GHDR 15-4 particles and a low amount of carbon additive. Indeed, the multiplication of points of contact between the composite electrodes and the current collector reduces the overall resistance at

the interface.[23],[24] Finally, within the porosity window of electrodes tested in batteries (32%-40%), we observe a small increase in the resistivity with increasing SiO_x content in the *y-SiO$_x$* series. This one remains however very low as the values vary between 1 and 4×10^{-3} Ohm cm².

3.2 Cyclability in Li||SiO_x Gr half cells

The lithiation specific capacities versus cycle number for the four electrodes are shown in Figure 3a. Please note that error bars are smaller than the symbol height. As expected, the specific capacity increases with the increase of SiO_x content. Its impact on the 1st cycle irreversible capacity loss is also as expected. The latter clearly increases with the SiO_x content. From cycle 2 to 60, the graphite reference electrode displays a very slow capacity fading (0.18 ± 0.00 mA h g^{-1} per cycle) whereas it is steeper for 23-, 30- and 40-SiO_x ones, respectively 1.64 ± 0.01, 1.76 ± 0.01 and 1.78 ± 0.03 mA h g^{-1} per cycle (Table 3). However, this fading is negligibly dependent on the SiO_x content. This result does not reflect the trend generally observed for which an increased capacity fading is typically observed when the content in Silicon-based materials or when the specific capacity of this one increases.[17],[18],[19]. This result is all the more remarkable in our eyes as it was obtained without any search for optimization of the formulation of the electrodes with a higher SiO_x content (30- and 40-SiO_x), starting from that optimized for that with a lower content (20-SiO_x), establishing the relevance of the formulation parameters that are the coverage Γ, contact Ω and percolation ratio δ. In complement, relative capacity versus cycles number are shown in Figure S1.

The coulombic efficiency (CE) for the first twenty cycles is plotted Figure 3b. The initial coulombic efficiency (ICE) decreases with the increase in SiO_x content, from 91.3 for the reference electrode to 71.9% for the 40-SiO_x one, which is congruent with the literature.[20],[21] Indeed, SiO_x has a low ICE of ≈ 50-70%, which is mainly due to irreversible electrochemical reaction of SiO_2 phase with lithium to form Li_4SiO_4, in addition to the electrolyte reduction and SEI formation.[20],[21],[25],[26] This poor ICE is identified as a barrier to the practical use of SiO_x in full-cells configuration in which the lithium source is limited. Then, CE values reach

97-99% for all *y-SiO$_x$* series at cycle 2, with an increase from 97.1% for 40-SiO$_x$ to 98.8% for graphite reference. Finally, all coulombic efficiencies are up to 99% from cycle 3 onwards. Figure 3c presents results of DCIR measurements, which will be discussed later.

Table 3: Specific capacity loss per cycle between cycle 2 and 60, calculated by linear fitting considering standard deviation, and the specific capacity at the 5th cycle for the SiO$_x$/graphite blend, graphite only and SiO$_x$ only (extracted from incremental capacity curves from the two latter).

	Specific capacity loss		Capacity at 5th cycle			
Name	Linear fit	R-Square	SiO$_x$/Graphite	Graphite	SiO$_x$	Corrected SiO$_x$[a]
	[mA h g^{-1} per cycle]	(COD)	[mA h g^{-1} $_{SiOx/Gr}$]	[mA h g^{-1} $_{Gr}$]	[mA h g^{-1} $_{SiOx}$]	[mA h g^{-1} $_{SiOx}$]
Graphite	-0.18 ± 0.00	0.965	362 ± 0	362 ± 0	/	/
23-SiO$_x$	-1.64 ± 0.01	0.997	611 ± 1	404 ± 1	1293 ± 8	1422 ± 5
30-SiO$_x$	-1.76 ± 0.01	0.996	699 ± 3	440 ± 5	1289 ± 3	1469 ± 5
40-SiO$_x$	-1.78 ± 0.03	0.988	809 ± 2	491 ± 4	1273 ± 6	1470 ± 4

[a] Corrected SiO$_x$ capacity at 5th cycle is calculed by fixing the graphite one at 360 mA h g^{-1} $_{Gr}$.

Representative potential vs. relative capacity profiles for *y-SiO$_x$* electrodes after 5 cycles are shown in Figure 3d. On one hand, the graphite electrode displays typical symmetrical lithiation/delithiation curves reacting at low potential versus lithium. On the other hand, 23-, 30- and 40-SiO$_x$ curves are all similar but different from that of graphite except between 80 and 100% relative capacity (or state of charge, SOC), depending on SiO$_x$ content. This SOC range corresponds to the potential range where most of the graphite reactions with lithium occur. That is why this common part is decreasing with the increase SiO$_x$ content. Higher potentials correspond mostly to the potential range attributable to SiO$_x$. While 23-, 30- and 40-SiO$_x$ curves look quite similar during lithiation, clear differences appear during delithiation. This highlights the asymmetry of potential of reaction between the SiO$_x$/Gr electrode during lithiation step and the delithiation one as reported in the literature.[27],[28]

The different redox potentials and mechanisms of SiO$_x$ and graphite are better highlighted on incremental capacity curves, which are shown at cycle 5 in Figure 3e. While redox mechanisms overlap during the lithiation process, a more marked, although not complete, separation appears during delithiation, between the potential range corresponding to the electrochemical activity of graphite (below ≈ 290 mV at D/5) and that reflecting the activity

of SiO_x (above ≈ 290 mV). It testifies of a clear two-step delithiation, first graphite then SiO_x, as previously shown.[29],[30] In Figure 3e, a clear decrease of the graphite signature (light grey area) and increase in SiO_x one (light pink area) when the SiO_x/Graphite balance increases is seen. Using a home-made code on Python™, a direct integration of the area under the $dQ\ dV^{-1}$ vs Voltage curve during delithiation in each potential area yields an approximation of the capacities of SiO_x and graphite active materials (See Figure S2 for more details). Values at cycle 5 are reported in Table 3. The so-evaluated values are fairly consistent with the nominal capacities of each active material (≈ 360 mA h g^{-1}_{Gr} for graphite and ≈ 1400 mA h g^{-1}_{SiOx} for SiO_x). However, the so-calculated capacity in graphite area increases with the amount of SiO_x from ≈ 404 mA h g^{-1}_{Gr} to ≈ 491 mA h g^{-1}_{Gr} for 23- and 40-SiO_x electrodes respectively. These capacities are clearly too high to be attributable to graphite active material only. On the opposite, the capacity measured in the SiO_x area decreases with SiO_x content (Table 3). In fact, close inspection shows that SiO_x material provides 21% of its capacity in the potential range dedicated to graphite (under ≈ 290 mV), when graphite provides 5% of its up to 290 mV (more details in Supporting information Figure S2). This is expected to lead to an underestimation of the capacity of SiO_x material and an overestimation of that of graphite, as observed Table 3. These values nevertheless suggest that the two materials are still functioning at full capacity in this 5th cycle. Considering the expected specific capacity of 360 mA h g^{-1}_{Gr}, the specific capacity of SiO_x was back calculated to be 1422, 1469 and 1470 mA h g^{-1}_{SiOx} for 23-, 30- and 40-SiO_x electrodes respectively (Table 3). This back-calculation is in agreement with the over- and underestimation of our routine process based on incremental capacity analysis (See Figure S2c-d).

The capacity fading of SiO_x/Gr electrodes is known to come from the disconnection of SiO_x material from the electrode electrical network whereas graphite material better remain electrically percolated and thus electrochemically active. Two hypotheses are proposed in the literature: SiO_x particles are (i) mechanically isolated from surrounding particles due to their swelling/shrinking during electrochemical cycling[27],[31],[32] and/or (ii) passivated by the continuous creation of solid electrolyte interphase (SEI)[33]. During our previous study on 23-SiO_x electrodes we observed that both mechanisms are at work, but that mechanical

disconnection is the main cause of fading. Indeed, the latter is affected by the formulation of the electrode, namely the quantity of binder which affects the mechanical strength, and the composition of the mixture of graphite and conductive additive which affects, together with the porosity, the number of contacts between the carbon and the SiO_x phases.[15],[16]

3.3 Fading mechanism in Li||SiO_x Gr half cells

In order to study the fading mechanism, the incremental capacity curves were used to calculate the capacity delivered by each material (more precisely the capacity resulting from the potential ranges which are characteristic of them) throughout cycling, following the same methodology than above, except that the specific capacity of SiO_x was not back corrected. The results are shown in Figure 3f. In addition, direct current internal resistance (DCIR) measurements were done every ten cycles and are reported Figure 3c. Finally, SEM observations carried out on the 40-SiO_x and 23-SiO_x electrodes after 60 cycles are presented in Figure 4 and Figure S3, respectively. Moreover, Table 4 gives the thicknesses of representative electrodes measured before and after cycling.

Figure 3f shows that the graphite fully retains its capacity. The capacity vs cycle number curve is remarkably stable, meaning all particles remain electrochemically active and thus electrically connected, at least up to 45 cycles. While the SiO_x does not display a fading, in agreement with the already observed mechanism where some particles are mechanically and therefore electrically disconnected, leading to their electrochemical inactivation.[15],[16] Figure 3c shows the variation of the internal resistance of the cell. This one is measured with a short pulse of current to evaluate the electrical resistance of the electrodes without being affected by diffusion limitations of electrolyte species. All of 23-, 30- and 40-SiO_x electrodes display a quite similar internal resistance $\approx 12.7 \pm 0.4$ Ohm cm^{-2} at an early stage of cycling (here measured at cycle 14) which then linearly increases. While the internal resistance for the 23-SiO_x exhibits a slower increase up to 16.4 ± 0.3 Ohm cm^{-2}, the 30- and 40-SiO_x electrodes seem to show a steadier increase up to 19.6 ± 1.7 and 18.7 ± 2.3 Ohm cm^{-2} respectively. Nevertheless, the standard deviations are very large, making a clear distinction difficult. Thus, the study of internal measurement allows here only to confirm the increase of

internal resistance upon cycling without a clear discrimination based on the content of SiO_x. It is however remarkable that the evolution of the internal resistance is little dependent on the SiO_x content, with regard to their expected differences in dilation. Nevertheless, this result is in agreement with the absence of difference in the fading of these electrodes, and once again underlines the relevance of the adjustment of their formulation with the Γ, Ω and δ parameters. It can be observed that the internal resistance for the graphite electrode is initially superior to the others, which could be related to its higher current collector/electrode contact resistance (Figure 2b). This could also be related to the differences in charge transfer resistance of SiO_x and graphite.

Figure 4 and Figure S3 show different observations made on cross-sections of the 40-SiO_x and 23-SiO_x electrodes, respectively. Note that these observations were however done on electrodes of *y-SiO$_x$* series after D- and C-rate study (see section 3.3). In backscattered electron mode images, the different phases stand out more clearly due to their difference in density. The SiO_x appears light gray and the carbon phase dark gray. In Images in secondary electron mode, we can better see the topographical details. In view of the theoretical volume change of + 140% for lithiated SiO_x particles, the global structure of the two electrodes appears well preserved after cycling. The evolution of the morphology of the 23-SiO_x electrode has already been described in our previous work which focused on this composition. In summary, and for the electrode considered here, voids form around the SiO_x particles. In addition, the surface of the initially smooth SiO_x particles becomes rough, the result of the presence of the deposit formed by the SEI and also of a dissolution of the surface silicates, as shown by Richter et al.[34],[35] These degradations are illustrated in Figure S3. In the case of the 40-SiO_x electrode, when comparing to the pristine state (Figure 4a-b), the images after cycling indicate the same phenomena of formation of voids around the SiO_x particles, (see for example Figure 4c-d), presence of an SEI type deposit on the surface of the SiO_x particles (Figure 4c-d), and a surface roughness suggesting a dissolution of the material at its surface (Figure 4e).

An additional mechanism is observable for this electrode richer in SiO_x, the formation of cracks parallel to the current collector (Figure 4f). This mechanism, very different from that

observed in silicon-rich electrodes, where cracking occurs perpendicular to the current collector,[36],[37] was also observed by Profatilova et al.[38] for negative electrodes containing 7 wt% silicon (capacity 500 mA h g^{-1}). This cracking mechanism observed for the 40-SiO_x electrode is attributable to the higher SiO_x content which must induce greater expansion of this electrode, compared to 23-SiO_x which contains less SiO_x, and the coalescence (percolation) of the voids created around the SiO_x particles. In our previous works, we observed that electrodes with high content of SFG6L graphite are more subject to exfoliation parallel to the current collector due to the orientation of the SF6L platelets.[16] It is important to note that these observations are carried out on electrodes free of any mechanical constraint, whereas in electrochemical cells (button cell in this case), a pressure is exerted, of the order of 0.1-0.5 MPa,[39] which can counteract the opening of these cracks and maintain more or less electrical contact between the electrode layers on either side of these cracks.

Table 4: Electrodes thicknesses, areal capacity and expansiona between pristine state and after D/C rate study (67 cycles) for y SiOx series.

Sample	Thickness [µm]				Initial areal capacity	Expansion[a]
	Pristine	1 cycle	After cycling	Increase	[mA h cm^{-2}]	[µm mA^{-1} h^{-1}]
Graphite	105 ± 4	-	122 ± 3	+18 ± 3	5.00 ± 0.00	2.0 ± 0.3
23-SiO_x	71 ± 3	80 ± 4	090 ± 3	+18 ± 0	5.19 ± 0.04	2.0 ± 0.0
30-SiO_x	69 ± 5	-	092 ± 3	+22 ± 3	5.36 ± 0.05	2.3 ± 0.3
40-SiO_x	60 ± 2	74 ± 3	088 ± 0	+29 ± 3	5.29 ± 0.01	3.1 ± 0.3

[a] Electrode thickness increase per its initial capacity (A h). This calculation allows us to eliminate the differences in mass loading between electrodes.

Thickness variation has been monitored for the various electrodes at different states of cycling (Table 4). A trend is expected to be observed as a function of the number of cycles even though electrodes tend to naturally expand once they are recovered from the cell and no longer undergo the pressure exerted by the battery spring. As discussed above, the electrode thickness decreases as the content of SiO_x in the electrode increases. After cycling, the initial 105 µm of graphite electrode thickness are increased by 18 µm (+17%), the 71 µm of 23-SiO_x by 18 µm (+25%) and the 60 µm of 40-SiO_x by 29 µm (+48%). Moreover, 23- and 40-SiO_x electrodes were also disassembled after one complete cycle and it is interesting to

see that expansion is already of +9 µm (+13%) and +14 µm (+23%) respectively. Thus, a significant part of the expansion is already reached after one cycle, as observed in the literature.[40],[41] Although we were aiming for an areal capacity of 5.2 mA h cm^{-2} for all the compositions, the reality in the laboratory makes it difficult to achieve such precision during the coating of the electrodes, as can be seen from the actual values (Table 4). In order to rationalize electrode expansions in relation to the expected expansion with regard to a similar areal capacity, this swelling (in µm) is normalized by their initial capacity (in mA h) to give a measurement of their expansion which is expressed in µm mA^{-1} h^{-1}. The values are 2.0 ± 0.3, 2.0 ± 0.0, 2.3 ± 0.3 and 3.1 ± 0.3 µm mA^{-1} h^{-1} for graphite, 23-, 30-, and 40-SiO_x, respectively. The expansion coefficients are close for the graphite electrode and for the one containing 23%^{wt} SiO_x, which is an indication that the formulation optimized for the latter is efficient, giving this electrode a certain ability to accommodate and buffer variations in SiO_x volume. As expected, the expansion coefficient of the electrodes increases with increasing SiO_x content and one would have expected an aggravated degradation of these electrodes. However, the electrochemical results of cyclability (Figure 3) show quite similar capacity fading for the 23-, 30- and 40-SiO_x electrodes. This once again reinforces the relevance of the coverage Γ, contact Ω and percolation δ ratios for electrode formulation optimisation. The clear trend observed in terms of the relative expansion with SiO_x content is a problem for their integration in industrial rigid casing which must consider empty spaces to allow for the volume expansion of Si/SiO_x materials. In particular, it has even been shown that it is not worthwhile adding more than 40%wt of SiO to the anode, otherwise these needed empty spaces, which completely level out the gain in volumetric energy (W h L^{-1}).[21] However, electrodes in coin cell configuration are operated under pressure (finite volume, springs etc.). This means that mechanical relaxation of the electrodes after coin-cells opening cannot be ruled out and may have an impact on these conclusions.

Finally, we would like to comment on the evolutions of the capacity delivered by each material, as calculated from incremental capacity curves (Figure 3d), above 40 cycles, where it can be seen that the capacity delivered by graphite starts declining while that by SiO_x stops declining. Figure 3g displays an example of the evolution of the incremental capacity for the

40-SiO_x electrode upon cycling. The graphite peaks shift to a lower potential in lithiation and to a higher potential in delithiation, showing the growing of the cell polarization, in agreement with DCIR measurements, likely due to the continuous irreversible expansion of the electrode and the growth of the SEI, which increase the electrode resistance. A polarization also manifests itself on the SiO_x first peak in lithiation (at ~250 mV) that shifts to a lower potential upon cycling. However, in delithiation, the pattern is strikingly different. One has to remind that the (de)lithiation of amorphous silicon, here the silicon nanodomains in the SiO_x particles, is a two-step process.[42],[43] In lithiation, lithium poor and then lithium rich alloys form, while in delithiation it's the opposite, first lithium rich alloy delithiate to form lithium poor alloy, which then delithiate to form silicon. In delithiation, these two steps lead to the two large peaks at ~300 and ~500 mV, respectively. While the first step appears more intense at the beginning of cycling than the second one, this trend tends to reverse upon cycling. There is a decrease of the incremental capacity below 400 mV coupled with an increase between 400 and 500 mV after cycle 40. The fingerprint of the incremental curve is however unaffected in lithiation and there is also no particular change in the slope describing the capacity fading (Figure 3a and Table 3) indicating that there is no particular additional process that would be linked to a specific capacity loss. In addition, the profile of the incremental capacity for the 40-SiO_x electrode at low potential (grey area) in particular at the expected redox potential of stage 1 of graphite (≈ 270 mV) tends to resemble that of pure graphite reference. On the other side, at higher potential (red area), the incremental capacity profile above 550 mV seems unchanged upon cycling ruling out simple kinetics limitation that would shift the entire incremental capacity profile towards higher potential. Furthermore, this phenomenon is weakly observed for the 20-SiO_x electrode but more marked for 30- and 40-SiO_x although it does not appear at the same stage of cycling (see all curves in Figure S4) which explains the large standard deviation above 40 cycles. This phenomenon does not seem to be specific to our electrodes, since this signature can be found in some papers in the literature.[32] As this phenomenon is only observed in delithiation and is dependent on the quantity of SiO_x in the electrode, we believe that it does not reflect a structural evolution of the material, which would change the mode of electrochemical reaction, but that this is rather

due to the morphological modifications induced within the electrode by the expansion and contraction of the SiO_x particles. The mechanism we are thinking of is as follows. During delithiation, the SiO_x particles efficiently connected to the graphite matrix will begin to delithiate, which will create voids in the electrode and even open cracks. This can delay other SiO_x particles delithiation. However, with the appearance of voids in the electrode following the contraction of the first SiO_x particles, the mechanical resistance of the electrode to the compression exerted by the spring may weaken, and the electrode collapse on itself, closing the open cracks, allowing the delithiation of the SiO_x particles which had not been able to do so at a lower potential. This hypothesis is inspired by dynamic behavior observed on certain silicon[31] and silicon/graphite electrodes[44] which also present an original breathing phenomenon. Advanced in situ or operando characterizations are needed to clarify the aging mechanism of SiO_x-based electrodes.

To conclude this part, the main cause of the capacity fading seems to be the same for all electrode formulations studied here, the expansion of the electrode which is all the more intense than the SiO_x content in the electrode increases. This expansion leads to a disconnection of SiO_x material upon cycling. However, while the silicon oxide content is increased in *y-SiO$_x$* series electrodes, they all display a similar capacity fading trend (Figure 3a) and increase of internal resistance (Figure 3c), because their formulations were adjusted to mitigate SiO_x disconnection. In our eyes, this supports the relevance of the concepts of coverage ratio Γ (Equation 1)[15], carbons to silicon ratio Ω (Equation 2)[16] and percolation ratio δ (Equation 3) in facilitating the design of optimized SiO_x-based electrodes architectures.

3.4 Rate performance in Li||SiO_x Gr half cells

The study of electrochemical cycling revealed a quite similar cyclability for 23-, 30- and 40-SiO_x electrodes despite the increase in silicon oxide content. The use of optimized values for the coverage, contact and percolation ratios enabled maintaining these performance. Nevertheless, formulation changes implied adjustments in binder content (PAA)[15], flake graphite (SFG6L)[16], and carbon additive (Table 1). Our previous work showed that an abusive use of smaller graphite such as SFG6L could in fact limit ionic diffusion due to the

formation of smaller pore size and higher tortuosity in the electrode architecture. As the SFG6L content is increased in 40-SiO_x electrode compared to 23-SiO_x, it raises the question of performance at higher cycling rates of both electrodes. Figure 5a-b show specific and areal capacities upon cycling at different cycling rates, respectively. In the following and for clarity purpose, the cycling rate is referred as C-rate during lithiation and D-rate during delithiation. After the three formation cycles at C/20-D/20, a first part between cycle 4 and 34 is dedicated to the D-rate effect (D/5, D/2, 1D, 2D and 3D blocks), with the corresponding lithiation rate fixed at C/5 and ending with constant voltage (CV) step at 10 mV (see experimental section). The second part from cycle 35 to 64 is dedicated to the C-rate effect (during lithiation – same blocks but all without CV step), with the corresponding delithiation rate fixed at D/5. Some complete cycles at C/5-D/5 are interleaved between D- and C-rates blocks to assess the electrode integrity (check cycles). As observed in our previous work with electrodes containing 23%^{wt} of SiO_x, electrochemical performance are more affected by C-rate increase than D-increase.[16] We were also able to show that the capacity loss observed at high rate is not due to intrinsic degradation of the electrode but rather to electronic and/or ionic kinetics limitations. Figure 5c gives an overview of the relative capacity as a function of the D- or C-rate for the different electrodes and typical discharge and charge curves obtained during the D- and C-rate blocks are shown Figure S5.

Effect of D-rate during delithiation.

The addition of SiO_x in the electrode composition has clearly an impact on the capacity when the rate of cycling is increased. Interestingly, areal capacities are similar and barely impacted for slow delithiation rate up to a 1D rate (Figure 5b), with a relative capacity reaching 94% for all compositions (Figure 5c). Differences appears at 2D, where relative capacities (Figure 5c) are ≈ 65% for both graphite and 23-SiO_x electrodes, whereas 30- and 40-SiO_x with higher silicon oxide content decrease to ≈ 48%. At 3D, all electrodes with SiO_x deliver ≈ 10% of relative capacity. The graphite reference stands out at 41%. This result can be attributed to the lower operating voltage of graphite than SiO_x. Increasing cell polarization with increasing current will impact SiO_x more than graphite. Graphite has thus better ability to perform at high rate during the delithiation step than SiO_x.

In order to discriminate the capacity drops attributable to graphite and to SiO_x, a specific methodology had to be followed to evaluate D-rate effect (during delithiation) because the calculation of specific capacities stemming from graphite and SiO_x is done on delithiation profiles of incremental capacity. Details of this methodology are given in the Supporting Information (Figure S6 and Equation S1-2). The specific (Figure 5d) and areal (Figure 5f) capacities in delithiation of the graphite material of the composite electrodes are quite stable up to 2D and decrease to ≈ 100-150 mA h g^{-1}_{Gr} at 3D. Interestingly, the only electrode losing capacity on the graphite material at 2D is the pure graphite electrode. Numerous works have shown that the performance at high delithiation rate of high capacity graphite electrodes (> 3 mA h cm^{-2}) depends on the limitations imposed by the architecture of the electrode on the diffusion of the lithium salt in the electrolyte.[45],[46],[47],[48] These limitations are aggravated and performance reduced with increasing thickness and decreasing porosity of the graphite electrode. Please note here that the electrode loading increases with the decrease in SiO_x content to target an areal capacity of ≈ 5.2 mA h cm^{-2} (Table 2). In the case of the graphite electrode, this implies a much thicker electrode (Table 3) which has most probably an impact on ionic diffusion across the electrode thickness. This may explain this premature decrease of capacity of graphite electrode on the graphite material. On the opposite, only a slight decrease of capacity is measured for the SiO_x material from ≈ 1250 mA h g^{-1}_{SiOx} to ≈ 1150 mA h g^{-1}_{SiOx} between D/5 and 1D. A significant drop is then observed at 2D to reach 362, 183 and 211 mA h g^{-1}_{SiOx} for 23-, 30- and 40-SiO_x respectively. This order of performance is in agreement with observations made on electrode resistivity (Figure 2) and internal resistance (Figure 3c). In conclusion, even if the graphite electrode is thicker, resulting in more severe lithium salt diffusion limitations, the higher operating voltage of SiO_x is the most significant issue of SiO_x/graphite electrode to better perform at high delithiation rate than graphite electrode.

Effect of C-rate during lithiation.

Contrarily, SiO_x/graphite electrode better perform at high lithiation rate than graphite electrode. Indeed, graphite electrode can achieve ≈ 35% of relative capacity while electrodes containing SiO_x still reach ≈ 50% at C/2 (Figure 5c). This advantage is still noticeable at 1C

(≈ 10% and ≈ 19% for graphite and SiO_x electrodes, respectively). All relative capacities are ≈ 5% and ≈ 3% at 2C and 3C respectively and there is not any major differences between graphite, 23-, 30- and 40-SiO_x electrodes performance. During lithiation (reduction) and for graphite electrodes, the phenomenon affecting the most the ohmic drop in a half-cell is the one at the lithium electrode, which starts to be significant from current density of ≈ 1 mA cm^{-2} and higher.[46] In the present study, such current densities are effectively achieved at C/5 to reach ≈ 15 mA cm^{-2} at 3C (Table S3) due to the high areal capacity of ≈ 5.2 mA h cm^{-2} of the electrodes. For both graphite and SiO_x materials, specific (Figure 5e) and areal (Figure 5g) capacities strongly decrease in a similar way, likely because the ohmic drop originating from the lithium electrode affects both material reactions similarly. However, their difference in operating voltage makes a strong difference in their efficiency at high rates. Indeed, capacities delivered by the graphite material at C/2 are ≈ 100-150 mA h g^{-1}_{Gr} but close to zero at 1C. From C/5 to 1C, although the capacity of SiO_x material decreases steadily, specific capacities between 400 and 500 mA h g^{-1} are still delivered, confirming the better ability of this material to function at high lithiation rates due to its higher operating voltage. This gives a clear advantage for electrodes containing SiO_x active material up to 1C.

Unfortunately, several parameters vary between the different compositions (Table 1) in order to keep the different ratios constant (Equation 1-2-3), which makes difficult to compare the *y-SiO$_x$* series electrodes directly to each other. Indeed, as the SiO_x/Graphite balance becomes richer in SiO_x, it leads to the use of more small-sized graphite (SFG6L), more binder (PAA) and more conductive additive content (C45 and CNT). All these changes impact electrode thickness, porosity distribution and tortuosity, and to a lesser extent electrical properties, which influence charge transport and transfer properties in a convoluted way.

To conclude, (1) SiO_x-based electrode tolerate more the increase in cycling rate during delithiation step than lithiation; (2) the graphite component withstands the rate increase during delithiation better than SiO_x material, whereas the opposite is true for lithiation. Thus, the use of this type of anode may be appropriate for applications that do not require fast discharge but could have the advantage a faster charge than pure graphite electrode.

3.5 Cyclability in SiO_x Gr||NMC_{811} full cells and energy/power density considerations

In half-cell configuration, the volumetric and gravimetric capacities (mA h L^{-1}_{El} and mA h g^{-1}_{El}) at the electrode level remain clearly higher than that of graphite for SiO_x/Gr electrodes even after 60 cycles. + 28% volumetric and + 44% gravimetric capacities for 40-SiO_x (see Figure S7 and related comments in supporting information). To evaluate these electrodes in a situation closer to the application, cyclability tests were carried out in full-cell configuration for graphite, 23- and 40-SiO_x electrodes versus NMC_{811}-based positive electrode (see experimental section). As already explained with Figure 3b, an important issue of SiO_x is its poor initial coulombic efficiency (ICE), in agreement with the literature.[20],[21] Although it is not a problem in Li || SiO_x/Gr configuration due to the Li "infinite" reservoir of the lithium metal electrode, it becomes an unavoidable issue in full-cell configuration because a significant amount of lithium ions from the NMC material are trapped and thus lost in the silicates and SEI formation. The full capacity of the NMC-based cathode then cannot be reached anymore, as we already observed in our previous work.[15] Numerous studies have been carried out to pre-lithiate SiO_x material in order to overcome this problem.[20],[49],[50],[51] At lab scale in coin cell casing, the easiest way to have a prelithiated anode is certainly to perform one complete cycle in Li || SiO_x/Gr configuration before assembling it again in SiO_x/Gr || NMC_{811}, which was performed here (see experimental section and Figure S8a). This method implies to open the Li || SiO_x/Gr which may introduce potential biases such as extra degradation of the electrode during manipulation or electrode relaxation as the electrode is no longer held under pressure by the cell spring. In fact, it was on this opportunity that we measured the thickness of these electrodes after one cycle (Table 4).

The Figure 6a displays potential versus relative capacity curves of graphite, 23-, 40-SiO_x and NMC_{811} electrodes in half-cell configuration versus metallic lithium. These curves clearly illustrate the impact of replacing Li metal for SiO_x at the negative electrode side. Indeed, this material reacts at higher potentials than graphite versus lithium which reduces the difference of potential with a NMC_{811} positive electrode. This is confirmed with Figure 6b where cell voltage of full-cell SiO_x/Gr||NMC_{811} versus specific capacity are displayed at cycle 5. Real cell mean voltages of discharge of *y-SiO_x* || NMC_{811} batteries at D/5 are reported in Table 5 and decrease from 3.68 V to 3.56 and 3.51 V for graphite, 23-SiO_x and 40-SiO_x anode,

respectively. At the same time, this reduces the energy of the cell (at a rate of C-D/5) from 33.8 to 32.7 and 32.2 W h and its power from 6.77 to 6.55 and 6.44 W since the capacity of 5.2 mA h cm^{-2} of the batteries are similar and independent of the anode type. However, we also calculated the energy and power densities of these cells per mass and volume of both anode and cathode to extrapolate to commercial cells in which a reduction of electrode thickness allows to set more electrode layers in the cell casing and thus increases the cell capacity. Usually, these values are calculated using the specifications of all the battery components including separator, electrolyte and the casing, but this approach is not appropriate in coin cell configuration where the casing represent ≈ 90% of the total weight of the battery. Moreover, values in Table 5 can be of further use with other cell configurations, since we are only taking into account masses and volumes of the electrodes without their current collector. Gravimetric energy and power are increased by ≈ +13% for 23-SiO_x || NMC_{811} cell and by ≈ +17% for 40-SiO_x || NMC_{811} cell compared to Gr || NMC_{811} battery when volumetric energy and power are increasing by ≈ +18% and by ≈ +28%, respectively. Volumetric energy and power are trickier to estimate because the electrode usually swell upon cell cycling as shown in Table 4 and Figure S7. Finally, even though values in Table 5 can be reliable at a moderate rate of cycling, they should be taken with caution for higher discharge rates because in this case the increase in SiO_x content in graphite electrode decreases discharge capacities (Figure 5). As a result, the comparison of energy and power values between SiO_x-based and graphite-based electrodes will not be in favour of SiO_x-based electrodes as the rate of cycling is increased.

Table 5: Full cell performance in terms of energy (W h), power (W), gravimetric energy (W h kg^{-1}) and power (W kg^{-1}), volumetric energy (W h L^{-1}) and power (W L^{-1}) of graphite, 23- and 40-SiO_x anodes vs. NMC_{811} cathode.

Sample	Cell characteristics at C-D/5			Raw cell performance		Gravimetric[d]		Volumetric[d]	
	Theoretical areal capacity [mA h cm^{-2}]	Theoretical capacity [mA h]	Real discharge cell voltage[a] [V]	Energy[b] Discharge [mW h]	Power[c] Discharge [mW]	Energy [W h kg^{-1}_{El}]	Power [W kg^{-1}_{El}]	Energy [W h L^{-1}_{El}]	Power [W L^{-1}_{El}]
Graphite	5.2	9.2	3.68	33.8	6.77	399000	80000	7560000	151000
23-SiO_x	5.2	9.2	3.56	32.7	6.55	451 ± 0	90 ± 0	893 ± 41	179 ± 8
40-SiO_x	5.2	9.2	3.51	32.2	6.44	468 ± 3	94 ± 1	969 ± 23	194 ± 5

[a] Average cell voltage of discharge (V) at D/5 and 5th cycle is calculated from real energy (W h) divided by the

real capacity (mA h) of the cell. These values are averages of which the standard deviations are less than 0.2%. We have not included them in order to have a clearer view of values.

[b] Cell energy (mW h) is calculated from theoretical capacity (9.2 mA h) multiplicated by the cell voltage of discharge[a] (V).

[c] Cell power (mW) is calculated from the cell energy[b] (mW h) divided by the rate of cycling (5 h – D/5).

[d] Gravimetric and volumetric performance are calculated considering anode + cathode weights and thicknesses in their pristine state without current collector contributions.

Figure 6c displays the specific capacities per gram of NMC_{811} material versus cycle number for graphite, 23- and 40-SiO_x electrodes. Capacities measured just after formation cycles start at 187, 189 ± 0.2 and 190 ± 1.1 mA h g^{-1}_{NMC} respectively at cycle 4, they are then decreasing to 179, 173 ± 1.2 and 177 ± 1.6 mA h g^{-1}_{NMC} at cycle 60, which corresponds to capacity retentions of 94.7, 91.5 and 93.2%, respectively. Graphite||NMC full does not reached the cycle 60 for the moment, we did an estimation. Considering linear fading, we calculate an end of life of cycles 300, 130 and 170 cycles for Graphite, 23- and 40-SiO_x electrodes with the criteria of < 80% remaining capacity. The better capacity retention of 40-SiO_x compared to 23-SiO_x could be surprising but is in agreement with results obtained in half-cell configuration (Figure 3a).

4. Conclusions

The starting point of this work is a SiO_x/graphite electrode, whose mass ratio of active materials is 23:77, and whose performances had been previously optimized, by seeking an optimal formulation in terms of nature and quantity of additives non-electroactive (polymer binders and conductive agents) and in terms of nature and proportion of different graphites (platelet versus spherical). No less than 30 different formulations had been evaluated for this.[15],[16] This optimal formulation has been rationalized into three key parameters: the ratio of the mass of polymer binders to the surface area developed by all the powders (electroactive materials and conductive agents), the ratio of the surface area developed by the carbons (graphites and conductive agents) to the surface developed by the SiO, and the ratio of the surface developed by the conductive agents to the surface developed by the powders of the electroactive materials. These ratios have a physical meaning which is explained by the role of each of the constituents considered on the mechanical and electrical properties of the

matrix formed by the mixture of binders and carbon materials around the SiO_x, and on the durability of these properties during of cycling despite variations in volume of the latter.

Here, we have shown that these previously calibrated key parameters make it possible to directly identify, without any trial and error, SiO_x/graphite electrode formulations richer in SiO_x, with mass ratios 30:70 and 40:60, and which cycle just as good in terms of capacity retention as the first, in half-cell and even in full cell. This result is remarkable for several reasons: (i) because according to the state of the art, an increase in the silicon content in an electrode degrades its cyclability; (ii) always according to the state of the art because a modification of the electroactive material and its specific capacity requires numerous experimental tests to readjust the electrode formulation, which is an application obstacle. Key parameters in the formulation of SiO_x/graphite electrodes, and their critical values have therefore been identified in this work, which can be taken up and compared to other electrodes containing silicon-based materials different from that studied here. However, the porosity, the nature of the binder, and the nature of the graphites and conductive additives are likely to influence the critical values of these parameters. Thus, direct extrapolation to other silicon-based materials can only be undertaken by considering the same graphite, conductive additives, and binder, and similar electrode porosity to our work. Additional effort is required to arrive at more general parameters

Finally, the analysis of power performances, as well as the study of experimental gravimetric and volumetric energy and power densities underline the interest of these SiO_x-rich electrodes with regard to the graphite reference for lithium-ion batteries. For example, for the 40:60 mass ratio, at the 1C/1D charge/discharge rate, the charge capacity is increased by + 30% without alteration of the discharge capacity; the volumetric energy and power densities are increased by + 18 and + 28% compared to graphite; and finally, the capacity retention after 60 cycles only decreases from 94.6 to 93.1%.

Acknowledgments

M. Deleplanque and C. Busson are warmly thanked for fruitful discussions.

References

[1] M. Armand, P. Axmann, D. Bresser, M. Copley, K. Edström, C. Ekberg, D. Guyomard, B. Lestriez, P. Novák, M. Petranikova, W. Porcher, S. Trabesinger, M. Wohlfahrt-Mehrens, H. Zhang, *Journal of Power Sources* **2020**, *479*, 228708.

[2] M. N. Obrovac, V. L. Chevrier, *Chem. Rev.* **2014**, *114*, 11444.

[3] T. Chen, J. Wu, Q. Zhang, X. Su, *Journal of Power Sources* **2017**, *363*, 126.

[4] S. Chae, S. Choi, N. Kim, J. Sung, J. Cho, *Angew. Chem. Int. Ed.* **2020**, *59*, 110.

[5] X. Zhu, B. Liu, J. Shao, Q. Zhang, Y. Wan, C. Zhong, J. Lu, *Adv Funct Materials* **2023**, *33*, 2213363.

[6] B. L. Armstrong, K. A. Hays, R. E. Ruther, W. B. Hawley, A. Rogers, I. Greeley, K. A. Cavallaro, G. M. Veith, *Journal of Power Sources* **2022**, *517*, 230671.

[7] M. Wetjen, M. Trunk, L. Werner, R. Gernhäuser, B. Märkisch, Z. Révay, R. Gilles, H. A. Gasteiger, *J. Electrochem. Soc.* **2018**, *165*, A2340.

[8] J. Xiong, N. Dupré, D. Mazouzi, D. Guyomard, L. Roué, B. Lestriez, *ACS Appl. Mater. Interfaces* **2021**, *13*, 28304.

[9] K. Ambrock, M. Ruttert, A. Vinograd, B. Billmann, X. Yang, T. Placke, M. Winter, M. Börner, *Journal of Power Sources* **2022**, *552*, 232252.

[10] S. Yamazaki, R. Tatara, H. Mizuta, K. Kawano, S. Yasuno, S. Komaba, *Mater. Adv.* **2023**, *4*, 1637.

[11] M. J. Jolley, T. S. Pathan, Alan. M. Wemyss, I. Prokes, S. Moharana, C. Wan, M. J. Loveridge, *ACS Appl. Energy Mater.* **2023**, *6*, 496.

[12] Z. Du, R. A. Dunlap, M. N. Obrovac, *J. Electrochem. Soc.* **2014**, *161*, A1698.

[13] F. Jeschull, Y. Surace, S. Zürcher, G. Lari, M. E. Spahr, P. Novák, S. Trabesinger, *J. Electrochem. Soc.* **2020**, *167*, 100535.

[14] C. Wang, T. Ma, X. Liu, Z. Liu, Z. Chang, J. Pang, *Batteries* **2023**, *9*, 78.

[15] C. Meyssonnier, A. Merabet, N. Dupré, C. Paireau, B. Lestriez, *Small Methods* **2023**, 2301370.

[16] C. Meyssonnier, C. Chalard, N. Goubard, A. Merabet, N. Dupré, C. Paireau, B. Lestriez, *Batteries & Supercaps* **2024**, e202400119.

[17] Y. Oumellal, N. Delpuech, D. Mazouzi, N. Dupré, J. Gaubicher, P. Moreau, P. Soudan, B. Lestriez, D. Guyomard, *J. Mater. Chem.* **2011**, *21*, 6201.

[18] A. Tranchot, H. Idrissi, P.-X. Thivel, L. Roué, *Journal of Power Sources* **2016**, *330*, 253.

[19] M. Wetjen, D. Pritzl, R. Jung, S. Solchenbach, R. Ghadimi, H. A. Gasteiger, *Journal of The Electrochemical Society* **2017**.

[20] X. Li, X. Sun, X. Hu, F. Fan, S. Cai, C. Zheng, G. D. Stucky, *Nano Energy* **2020**, *77*, 105143.

[21] Y. Reynier, C. Vincens, C. Leys, B. Amestoy, E. Mayousse, B. Chavillon, L. Blanc, E. Gutel, W. Porcher, T. Hirose, C. Matsui, *Journal of Power Sources* **2020**, *450*, 227699.

[22] K. A. Striebel, A. Sierra, J. Shim, C.-W. Wang, A. M. Sastry, *Journal of Power Sources* **2004**, *134*, 241.

[23] N. Besnard, A. Etiemble, T. Douillard, O. Dubrunfaut, P. Tran- Van, L. Gautier, S. Franger, J. Badot, E. Maire, B. Lestriez, *Advanced Energy Materials* **2017**, *7*, aenm.201770043.

[24] C. Busson, M.-A. Blin, P. Guichard, P. Soudan, O. Crosnier, D. Guyomard, B. Lestriez, *Journal of Power Sources* **2018**, *406*, 7.

[25] K. Kitada, O. Pecher, P. C. M. M. Magusin, M. F. Groh, R. S. Weatherup, C. P. Grey, *J. Am. Chem. Soc.* **2019**, *141*, 7014.

[26] T. Hirose, M. Morishita, H. Yoshitake, T. Sakai, *Solid State Ionics* **2017**, *304*, 1.

[27] H. Pegel, O. Von Kessel, P. Heugel, T. Deich, J. Tübke, K. P. Birke, D. U. Sauer, *Journal of Power Sources* **2022**, *537*, 231443.
[28] M. Klett, J. A. Gilbert, K. Z. Pupek, S. E. Trask, D. P. Abraham, *J. Electrochem. Soc.* **2017**, *164*, A6095.
[29] K. P. C. Yao, J. S. Okasinski, K. Kalaga, J. D. Almer, D. P. Abraham, *Advanced Energy Materials* **2019**, *9*, 1803380.
[30] J. Moon, H. C. Lee, H. Jung, S. Wakita, S. Cho, J. Yoon, J. Lee, A. Ueda, B. Choi, S. Lee, K. Ito, Y. Kubo, A. C. Lim, J. G. Seo, J. Yoo, S. Lee, Y. Ham, W. Baek, Y.-G. Ryu, I. T. Han, *Nat Commun* **2021**, *12*, 2714.
[31] B. P. N. Nguyen, J. Gaubicher, B. Lestriez, *Electrochimica Acta* **2014**, *120*, 319.
[32] I. Choi, M. J. Lee, S. M. Oh, J. J. Kim, *Electrochimica Acta* **2012**, *85*, 369.
[33] T. Yoon, C. C. Nguyen, D. M. Seo, B. L. Lucht, *J. Electrochem. Soc.* **2015**, *162*, A2325.
[34] K. Richter, T. Waldmann, N. Paul, N. Jobst, R. Scurtu, M. Hofmann, R. Gilles, M. Wohlfahrt- Mehrens, *ChemSusChem* **2020**, *13*, 529.
[35] K. Richter, T. Waldmann, M. Kasper, C. Pfeifer, M. Memm, P. Axmann, M. Wohlfahrt-Mehrens, *J. Phys. Chem. C* **2019**, *123*, 18795.
[36] V. Vanpeene, J. Villanova, A. King, B. Lestriez, E. Maire, L. Roué, *Advanced Energy Materials* **2019**, *9*, 1803947.
[37] L. Huet, H. Houisse, N. Herkendaal, T. Devic, L. Roué, B. Lestriez, *Energy Tech* **2023**, *11*, 2201483.
[38] I. Profatilova, E. De Vito, S. Genies, C. Vincens, E. Gutel, O. Fanget, A. Martin, M. Chandesris, M. Tulodziecki, W. Porcher, *ACS Appl. Energy Mater.* **2020**, *3*, 11873.
[39] A. Smith, P. Stüble, L. Leuthner, A. Hofmann, F. Jeschull, L. Mereacre, *Batteries & Supercaps* **2023**, *6*, e202300080.
[40] Z. Karkar, D. Mazouzi, C. R. Hernandez, D. Guyomard, L. Roué, B. Lestriez, *Electrochimica Acta* **2016**, *215*, 276.
[41] D. Vidal, S. Genies, E. De Vito, M. Tulodziecki, W. Porcher, *Journal of Energy Storage* **2023**, *64*, 107174.
[42] M. Gauthier, D. Mazouzi, D. Reyter, B. Lestriez, P. Moreau, D. Guyomard, L. Roué, *Energy Environ. Sci.* **2013**, *6*, 2145.
[43] M. N. Obrovac, L. J. Krause, *J. Electrochem. Soc.* **2007**, *154*, A103.
[44] J. Xiong, N. Dupré, P. Moreau, B. Lestriez, *Advanced Energy Materials* **2022**, *12*, 2103348.
[45] H. Buqa, D. Goers, M. Holzapfel, M. E. Spahr, P. Novák, *J. Electrochem. Soc.* **2005**, *152*, A474.
[46] S. Malifarge, B. Delobel, C. Delacourt, *J. Electrochem. Soc.* **2018**, *165*, A1275.
[47] K.-H. Chen, M. J. Namkoong, V. Goel, C. Yang, S. Kazemiabnavi, S. M. Mortuza, E. Kazyak, J. Mazumder, K. Thornton, J. Sakamoto, N. P. Dasgupta, *Journal of Power Sources* **2020**, *471*, 228475.
[48] M. Parmananda, C. Norris, S. A. Roberts, P. P. Mukherjee, *ACS Appl. Mater. Interfaces* **2022**, *14*, 18335.
[49] Q. Meng, G. Li, J. Yue, Q. Xu, Y.-X. Yin, Y.-G. Guo, *ACS Appl. Mater. Interfaces* **2019**, *11*, 32062.
[50] M.-Y. Yan, G. Li, J. Zhang, Y.-F. Tian, Y.-X. Yin, C.-J. Zhang, K.-C. Jiang, Q. Xu, H.-L. Li, Y.-G. Guo, *ACS Appl. Mater. Interfaces* **2020**, *12*, 27202.
[51] T. Jia, G. Zhong, Y. Lv, N. Li, Y. Liu, X. Yu, J. Zou, Z. Chen, L. Peng, F. Kang, Y. Cao, *Green Energy & Environment* **2023**, *8*, 1325.

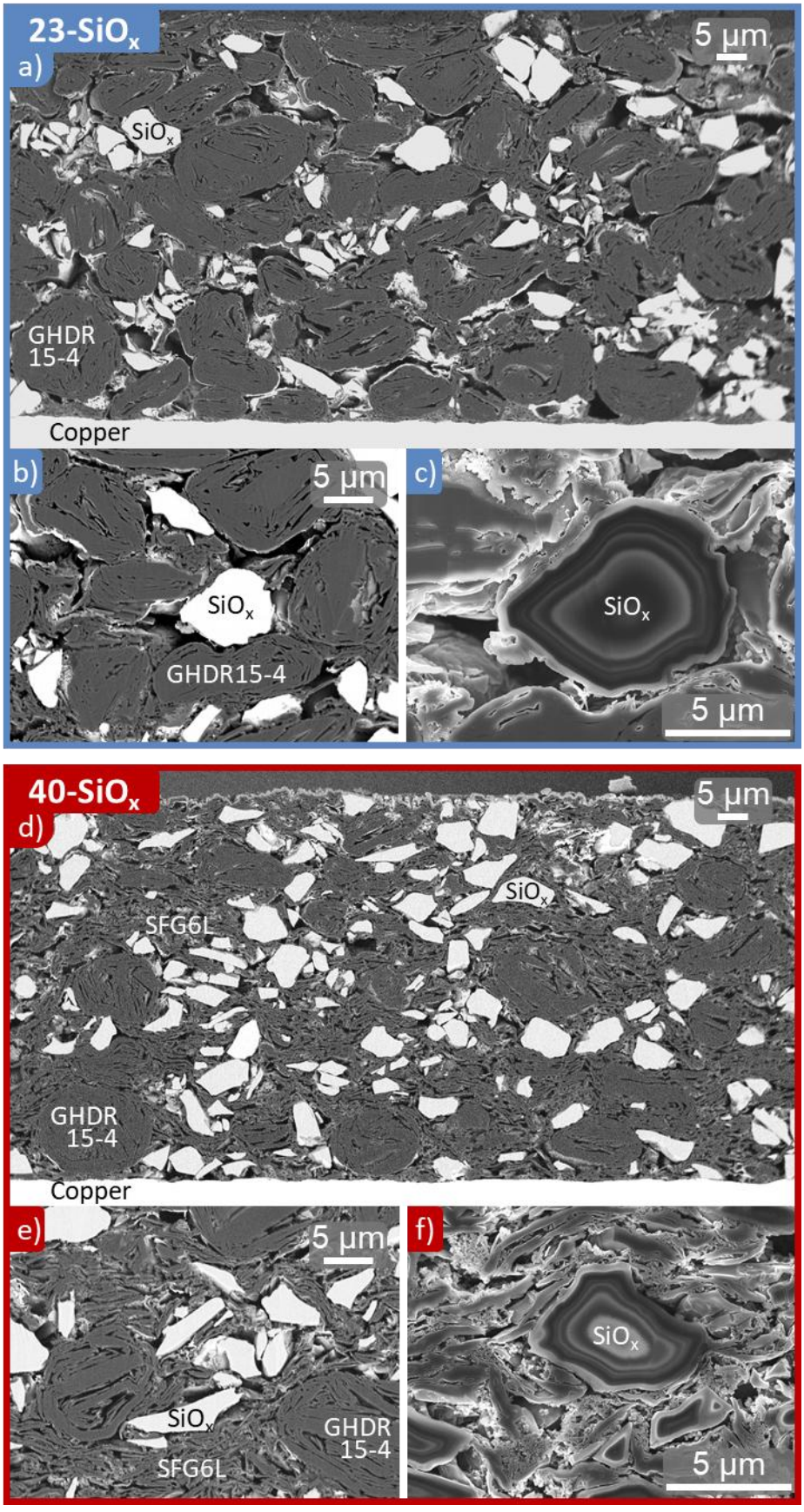

Figure 1: SEM observations of electrode cross section for (a b c) 23 SiOx and (d e f) 40 SiOx in backscattered (a b d e) electrons and in secondary electrons (c f).

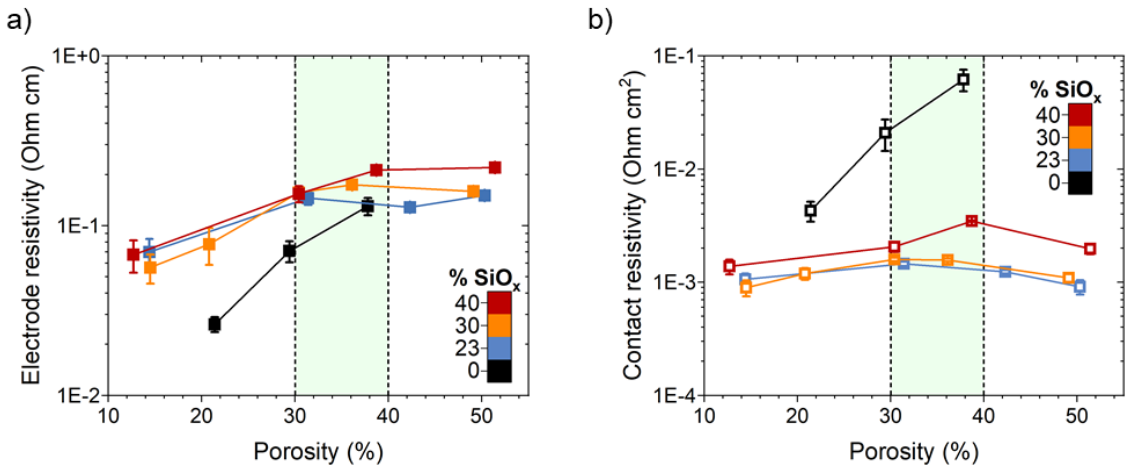

Figure 2: (a) Electrical resistivity of the electrode and (b) contact resistivity between the electrode and the current collector vs. porosity for y SiOx series. The green area delimits porosities of electrodes evaluated through electrochemical tests.

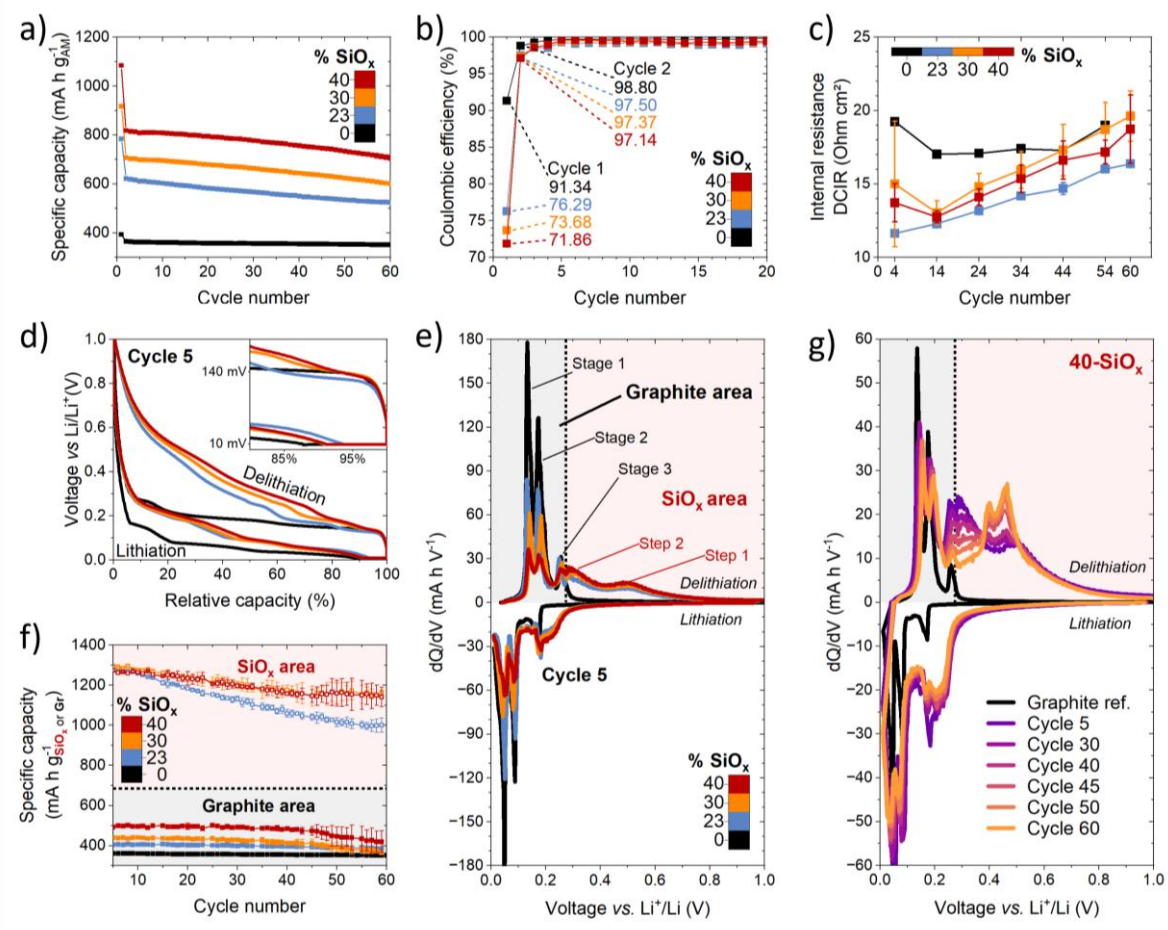

Figure 3: (a) Specific capacity, (b) coulombic efficiency and (c) Internal resistance by DCIR vs. Cycle number for y-SiO_x series; (d) Potential vs. relative capacity at cycle 5; (e) Typical dQ dV^{-1} curves vs. Cell voltage at cycle 5; (f) Specific capacity in the graphite and SiO_x potential windows obtained by incremental capacity analysis; (g) Example of dQ dV^{-1} curves vs. Cell voltage at different cycles for a 40-SiO_x cell.

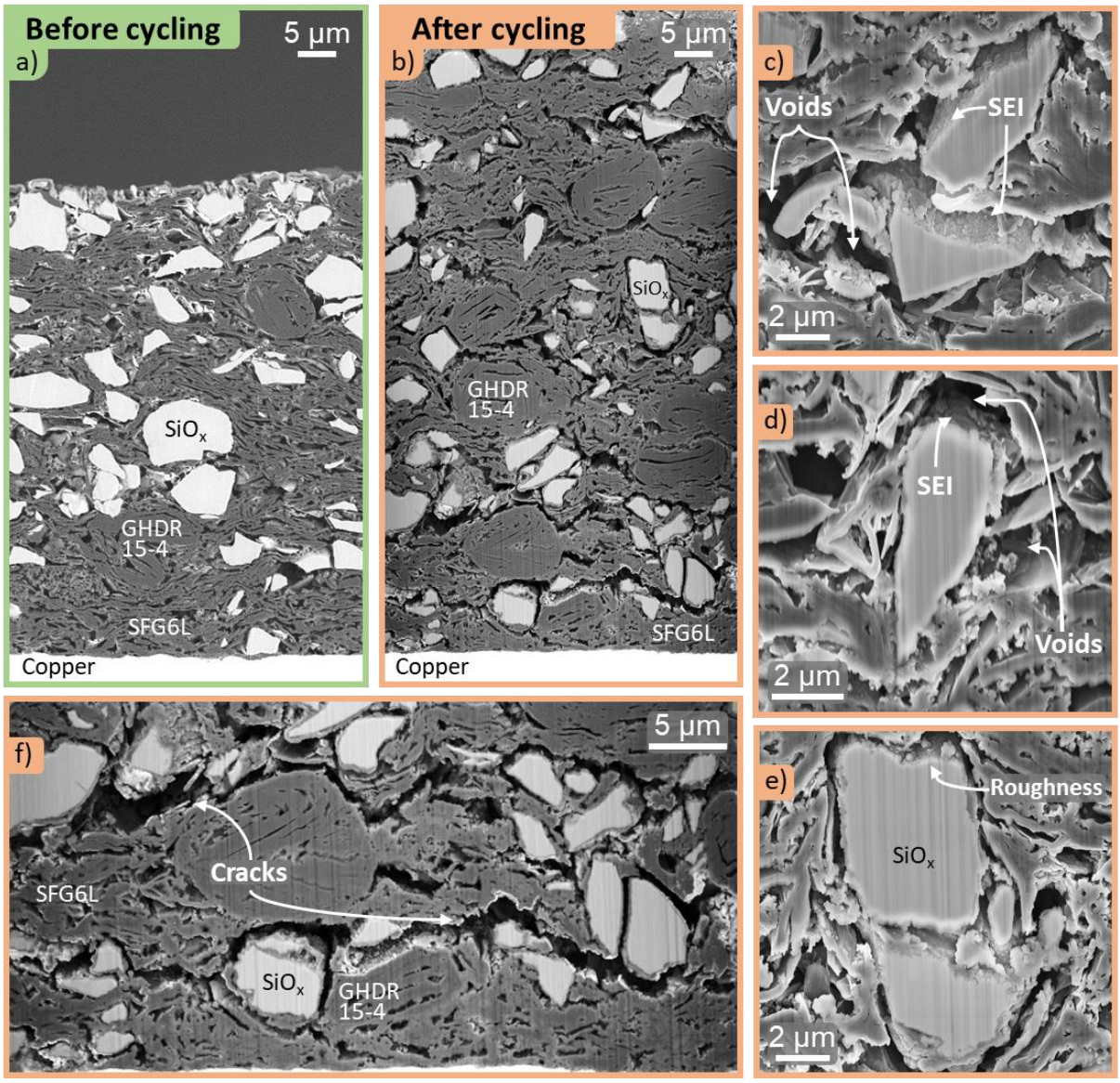

Figure 4: SEM observations of cross section of electrodes (a) before cycling and (b c d e f) after cycling for 40 SiOx electrodes in backscattered or secondary electrons.

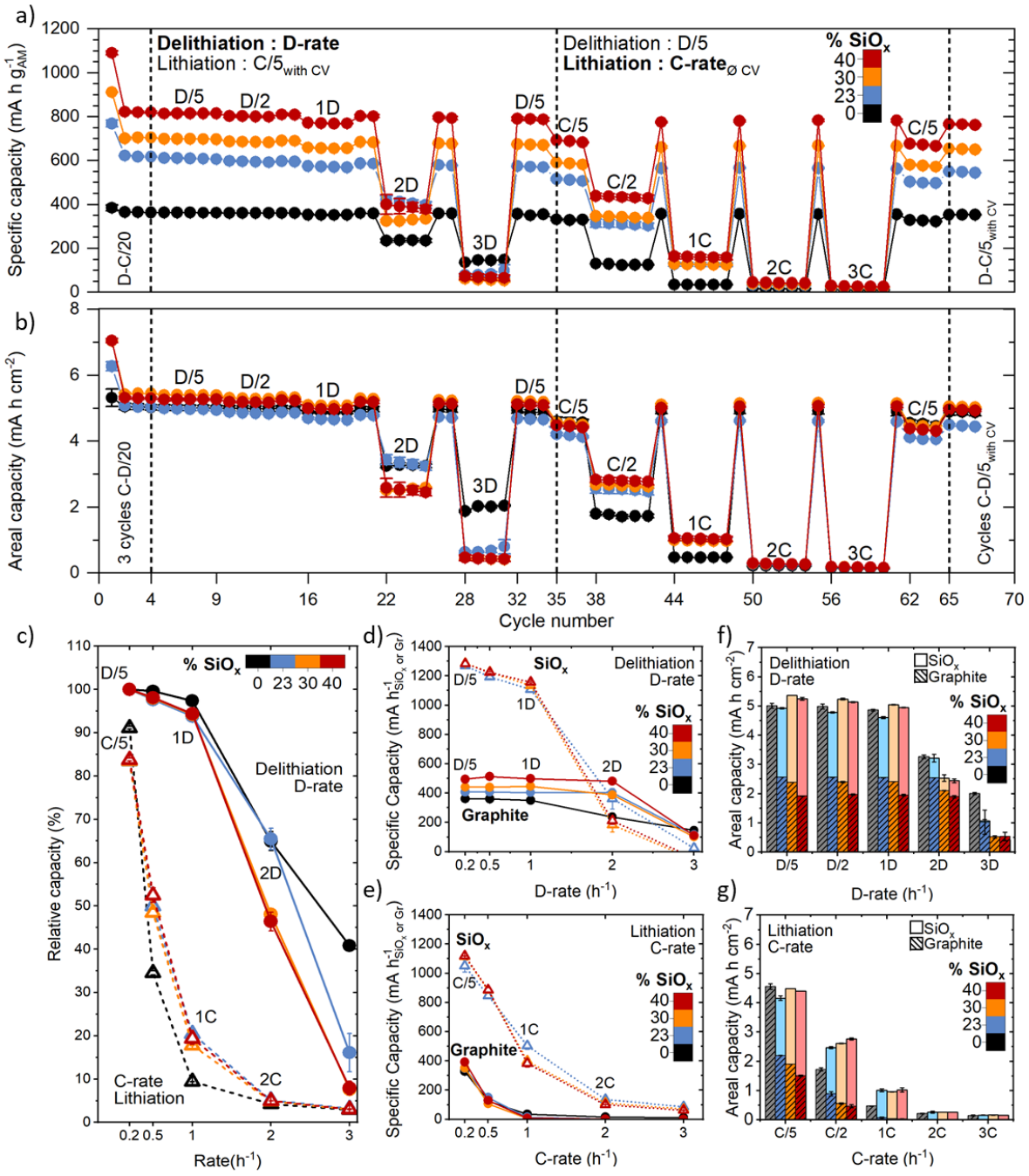

Figure 5: (a) Specific and (b) areal capacities vs cycle number at different D-rates but constant C/5 and then at different C-rates but constant D/5, for y-SiO_x series; (c) Electrode specific capacity vs cycling rate in delithiation and lithiation; Specific and areal capacities in the graphite and SiO_x potential windows vs cycling rate for different (d-f) D-rates and (e-g) C-rates.

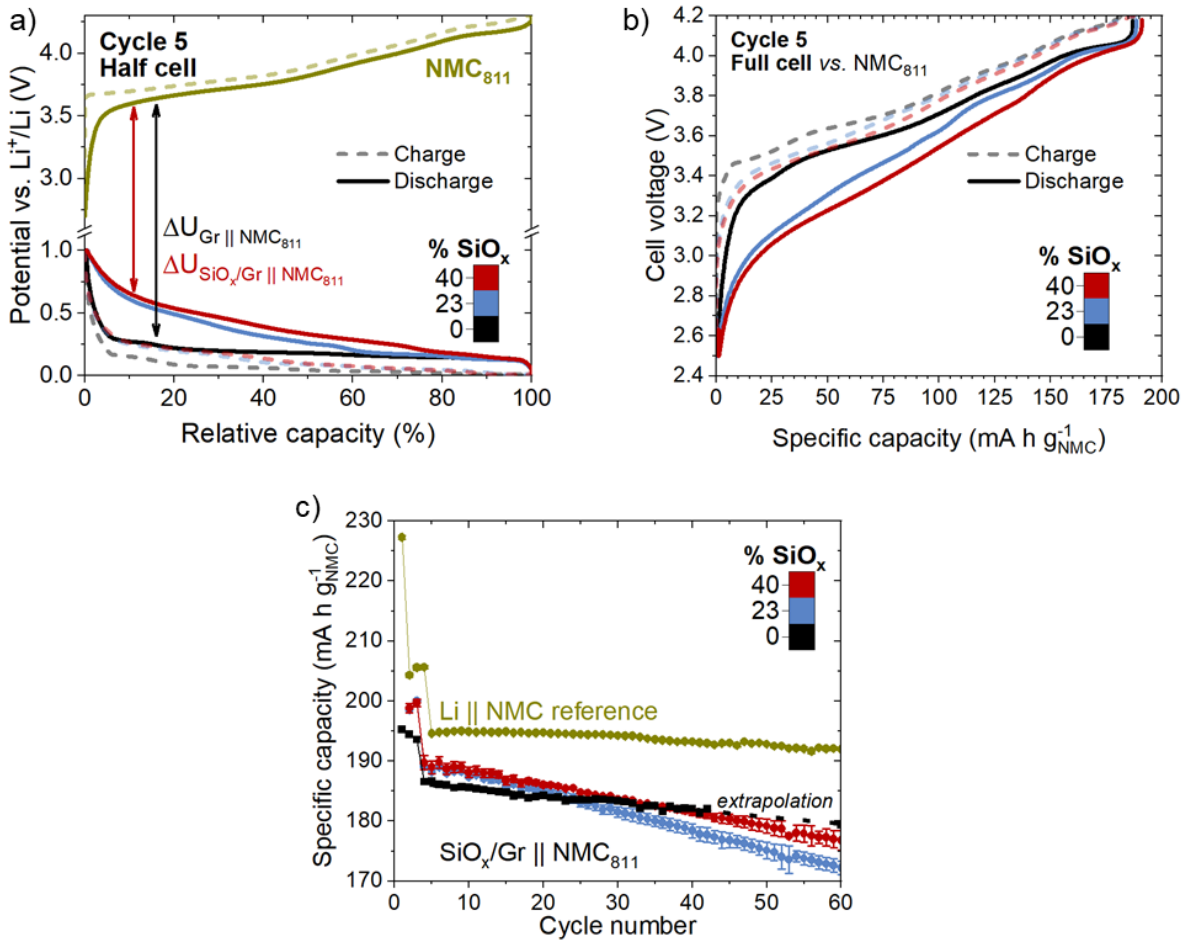

Figure 6: Potential vs. Relative capacity at 5th cycle of graphite, 23-, 40-SiO_x and NMC_{811} electrode versus (a) metallic lithium (half-cell), (b) Potential vs. Specific capacity per gram of NMC at cycle 5 of graphite, 23- and 40-SiO_x electrodes versus NMC_{811} cathode in which SiO_x-based electrode were prelithiated and (c) their *specific capacity vs. cycle number upon cycling.*